

**OPTICAL COUPLER DESIGN AND EXPERIMENTAL DEMONSTRATION FOR
2.5D/3D HETEROGENEOUS INTEGRATED ELECTRONICS**

A Thesis Proposal
Presented to
The Academic Faculty

By

Congshan Wan

In Partial Fulfillment
of the Requirements for the Degree
Doctor of Philosophy in the
School of Electrical and Computer Engineering

Georgia Institute of Technology

April 2018

Copyright © Congshan Wan 2018

TABLE OF CONTENTS

List of Tables	iv
List of Figures	v
Chapter 1: Introduction	1
Chapter 2: Literature Survey	2
2.1 Diffraction Grating Theory	2
2.1.1 Integral and Differential Method	3
2.1.2 Modal Approach	3
2.1.3 Rigorous Coupled-Wave Approach	4
2.1.4 Transmission Line Approach	4
2.1.5 Coupled Wave Theory	5
2.1.6 Perturbation Method	5
2.1.7 Coupled Mode Theory	6
2.1.8 Commercial PDE Solver	6
2.2 Optimization solver	7
2.3 Waveguide Grating Coupler Design	7
Chapter 3: Rectangular Grating Coupler: Efficiency Optimization and Angular Misalignment Analysis	9

3.1	RCWA-EIS Method	10
3.1.1	Step 1: Calculate Fields using Conventional RCWA	10
3.1.2	Step 2: Define Equivalent Index Slabs	11
3.1.3	Step 3: Calculate Radiation Factor	13
3.1.4	Step 4: Calculate Out-Diffraction Efficiency	13
3.2	Efficiency Optimization	14
3.2.1	Optimization Procedures	14
3.2.2	Results and Discussion	14
3.3	Angular Misalignment Analysis	18
3.3.1	Analysis Procedures	19
3.3.2	Results and Discussion	19
Chapter 4: Grating-Assisted-Cylindrical-Resonant-Cavities Interlayer Coupler: Theoretical Design and Experimental Validation		21
4.1	Theoretical Design	22
4.1.1	GARC Coupler Model	22
4.1.2	Simulation Results	24
4.2	Experimental Validation	26
4.2.1	Preliminary Results	27
Chapter 5: Proposed Work		29
5.1	Si/SiO ₂ GARC Coupler Fabrication and Verification	29
5.2	Innovative Fiber Alignment Fixture Design and Fabrication	31
References		35

LIST OF TABLES

2.1 Some reported SOI gratings for TE polarization. The column labels represent Si waveguide thickness (t_{Si}), grating period (Λ), grating etch depth (t_g), grating fill factor (f), grating line resolution (δ), grating length or dimension (L), single-grating efficiency (η_s), working wavelength (λ), and 1dB or 3dB bandwidth (1dB/3dB). CP, AP and DE represent chirped grating period, apodized fill factor, and double etch depths/widths, respectively.	8
.....	
3.1 Optimized parameters and calculated in-coupling/out-diffraction efficiencies for selected cases of binary gratings, parallelogramic gratings, saw-tooth gratings, and the volume gratings. $PC_{c,1}$ is the preferential coupling ratio, defined as the fraction of the total radiation power that is diffracted into the +1 order in the cover.	15
.....	
4.1 Parameter values for the optimized Si/SiO ₂ and Si ₃ N ₄ /SiO ₂ GARC couplers.	24
.....	
4.2 Via height d in μm for the (l,m) -th resonance at $1.55 \mu m$ free-space wavelength ($R = 7.0413 \mu m$) for the Si/SiO ₂ GARC.	26
.....	

LIST OF FIGURES

2.1 Optical losses present in rectangular gratings used for interlayer coupling. Possible solutions to reduce losses in a binary SOI grating out-coupler are (a)(b) increasing directionality to cover, (c) reducing back-reflection, and (d) reducing forward-transmission.	8
3.1 Schematic representation of (a) the grating in-coupling process and (b) the phase diagram based on the Floquet condition. This example shows multiple diffraction orders in the cover and substrate (not optimized for high efficiency), and the $i = -1$ order is a possible guided order whose propagation constant in the x direction is approximately equal to the guided mode propagation constant β in the waveguide.	10
3.2 Phase diagram of (a) the grating in-coupling and (b) the out-diffraction process with only the 0th and 1st orders. The light in-coupling into the 1st order in (a) is the reciprocal process of the guided wave out-diffraction into the 1st order in (b).	11
3.3 Schematic representation of field repetition outside of the grating by equivalent index slabs. (a) Electric field amplitude along the z direction of the multilayer grating structure, and (b) equivalent index slabs are used to replace the grating layer. It is not necessary to consider the fields inside the grating region.	12
3.4 In-coupling/out-diffraction efficiencies ($DE_{c,1}$) as a function of number of grating periods (N) for selected cases of optimized binary gratings, parallelogramic gratings, sawtooth gratings, and the volume gratings.	16
3.5 In-coupling/out-diffraction efficiencies ($DE_{c,1}$) as a function of number of grating periods (N) for optimized binary gratings with bottom grating reflector and metal reflector. Applying reflector results in twofold increase in diffraction efficiencies.	17
3.6 Schematic representation (not to scale) of the 3D interlayer grating coupling configuration under angular misalignment.	19

3.7	Bottom grating in-coupling efficiency as a function of rotation angle. For (a) and (b), N = 50; for (c), N = 30 (shorter grating due to geometric constrain under rotation).	20
4.1	Schematic representation of the GARC interlayer coupler. Two types of GARC structures determined by material systems (Si/SiO ₂ and Si ₃ N ₄ /SiO ₂) are shown.	22
4.2	Cross-sectional views of the optimized Si/SiO ₂ and Si ₃ N ₄ /SiO ₂ GARC couplers.	25
4.3	Spectral response for the optimized Si/SiO ₂ and Si ₃ N ₄ /SiO ₂ GARC couplers as well as that for the rectangular grating reported in [42].	25
4.4	Plot of efficiency as a function of via height for the Si/SiO ₂ GARC coupler.	26
4.5	SOI film thicknesses characterized by Woollam M2000 Elipsometer.	28
4.6	Si ₃ N ₄ film thickness characterized by Woollam M2000 Elipsometer.	28
4.7	VP-SEM images of gratings defined in the positive ZEP resist by ebeam lithography.	28
4.8	VP-SEM images of gratings defined in the negative IP-Dip resist by laser lithography.	28
5.1	Fabrication steps for the Si/SiO ₂ GARC coupler.	30
5.2	H_z field pattern at top of the via, assuming optical signal is launched from the bottom left waveguide. The field patterns at the top of the via are similar for the complete and half-completed structures.	30

CHAPTER 1

INTRODUCTION

The rapid growth of product sectors, such as data centers, 5G communications, augmented realities, and autonomous vehicles, etc., creates increasing demands for higher data rate and faster processing speed. Even though electronics have pushed their limits to satisfy these needs, heterogeneous integration with photonics is inevitable, as predicted by Integrated Photonic Systems Roadmap International (IPSR-I) [1]. This is because optical signals have many benefits such as large bandwidth, low energy, and small latency, etc. The emergence of 2.5D/3D integrated photonics offers opportunities for denser and more complex network designs without the problems of waveguide crossings and crosstalk. Interlayer optical couplers thus play a vital role in achieving efficient 2.5D/3D integrated photonics. Diffraction gratings are a common type of optical couplers because they can achieve relatively large interlayer distances and their planar geometries make them compatible with IC wafer-scale fabrication and testing. As research advances, it is possible that novel coupling structures will be designed to offer more choices for photonic system designs.

The objectives of this thesis proposal are to design, optimize and fabricate efficient optical couplers, including interlayer couplers and fiber couplers. In the first part, a new concept, the “equivalent index slab (EIS)” method, is proposed to extend the rigorous coupled-wave analysis (RCWA) to rectangular grating diffraction involving surface waves. The RCWA-EIS method is capable of optimizing rectangular grating couplers with arbitrary profiles and analyzing the effects of angular misalignments on the coupling efficiency. In the second part, a fundamentally new coupling structure, the grating-assisted-cylindrical-resonant-cavities (GARC) interlayer coupler, is proposed. The GARC couplers, based on cylindrical resonant cavities, have wider spectral bandwidth and higher coupling efficiency, which are promising alternatives to the conventional rectangular grating couplers.

CHAPTER 2

LITERATURE SURVEY

Diffraction gratings, which can be categorized as surface-relief gratings and volume holographic gratings, have many applications besides optical couplers. Surface-relief gratings, with variations in the surface profile, have been widely used in the field of photonics, (e.g. couplers [2, 3], polarizers [4], modulators [5], and switches [6], etc.) as well as other fields such as optoelectronics [7, 8], sensors [9, 10], and antennas [11]. With reduced thicknesses, planar geometries, and CMOS compatible materials, surface-relief gratings have become a popular solution in compact interconnect technologies. Volume holographic gratings, with variations in the refractive index of the material which are mostly polymer-based and glass-based, have been extensively explored in the field of data storage [12], optical correlation [13], optical information encryption [14], fiber communication [15], and spectroscopy [16], etc., due to their large bandwidth storage capability and high sensitivity in wavelength and angle. In order to fully exploit the benefits of diffraction gratings, it is important to study their diffraction behaviors using grating theories.

2.1 Diffraction Grating Theory

A number of theories have been proposed to study the grating diffraction phenomenon, including rigorous approaches and approximation methods. The rigorous approaches can be classified into two categories, namely the integral methods and the differential methods. The rigorous approaches usually gave numerically accurate results but sometimes they are computationally expensive, while approximation methods yield simpler but less accurate solutions. Nevertheless, all the theories start from the wave equation $\nabla^2 E + k^2 n^2 E = 0$ and represent the diffracted fields ($F = E_y$ or H_y) in a plane wave expansion (also called Floquet modal expansion or Rayleigh expansion) as $F(x, z) = \sum_{i=-\infty}^{\infty} C_i e^{jk_{x,i}x} e^{jk_{z,i}z}$.

2.1.1 Integral and Differential Method

The integral approach involves the resolution of an integral equation (and sometimes of coupled integral equations), while the differential method requires the resolution of an infinite system of coupled differential equations. The integral method was first developed to analyze the diffraction problem by perfectly conducting (metallic) gratings in the visible spectrum. As more advances in dielectric gratings in the UV and IR ranges take place, integral method becomes inadequate. Differential method was developed to study dielectric gratings and more complex objects in the spectral region where integral method is less efficient. Differential methods can be classified into two types: 1) representing fields using a suitable basis (for gratings, the periodicity of the fields leads to exponential basis) and casting the field expressions into a set of ordinary differential coupled equations (with one variable), and 2) discretizing the problem space into grids and direct solving partial differential equations (multiple variables) derived from Maxwell's equation at each grid point using a finite difference scheme [17]. The first type usually results in matrix formulations, and the numerical determination of these matrices usually governs the feasibility of the method. For the second type, the formulation is simple but requires long computing times and is limited by the numerical instabilities of the algorithm.

2.1.2 Modal Approach

Modal approach, a first type differential method based on eigenmode expansions, analyzes the diffraction problem in which a plane wave is incident on a grating bounded by two different media on two sides. In this approach, the grating is divided into layers featuring parallel interfaces. The permittivity varies only in the plane of the layer and is assumed to be constant along the perpendicular direction, allowing the separation of spatial variables. Within each layer the eigenmodes of the electromagnetic field are calculated and the general solution is then expressed by means of an eigenmode expansion [18]. The expansion coefficients can be found by solving the matrix equation generated by proper boundary

conditions. In practice, the expansion has to be truncated to obtain a finite dimensional matrix. The computation time of this method is generally low because all the calculations are explicit. The only time limiting step is the matrix inversion, which is based on the number of diffraction orders used. This method is only suitable for certain profiles, e.g. 1D gratings, while it is insufficient to treat profiles involving complicated 2D mathematics.

2.1.3 Rigorous Coupled-Wave Approach

The rigorous coupled-wave approach (RCWA) [19], also called Floquet modal method, has been used to analyze diffraction of both surface-relief gratings and volume gratings. It is based on the Modal approach but uses a different set of predetermined basis functions to express the fields in the grating. An advantage of the RCWA is that additional layers, e.g. a waveguide or another grating, can be added into the analysis. Due to its efficient computation inherited from the modal approach and its capability of analyzing waveguide grating structures, RCWA has become a popular theory to study diffraction gratings and it is also the basis theory used in this work. However, RCWA is typically applied to solve forward and backward diffraction in the plane normal direction and it is not applicable to surface waves (also referred as leaky wave due to attenuations) parallel to the interfaces. Therefore, leaky wave (RCWA-LW) approach and the proposed equivalent index slab method (RCWA-EIS) are suggested to analyze the waveguide grating in-coupling or out-diffraction where surface waves are involved. The comparison between RCWA-LW and RCWA-EIS will be discussed in Chapter 3.

2.1.4 Transmission Line Approach

Transmission line approach is similar to the RCWA except using voltages V_{mn} and currents I_{mn} to represent the coupled space harmonics in the grating layer. The parameter V_{mn} is related to I_{mn} via $V_{mn} = \sum_r Z_{m,n-r}^{(g)} I_{mr}$, where $Z_{m,n-r}^{(g)}$ is an impedance that represents the coupling of the r th harmonic of the magnetic field to the n th harmonic of the electric field.

The value of $Z_{m,n-r}^{(g)}$ is determined by the Maxwell's equations. Similarly, the parameters I_{mn} is related to V_{mn} via $I_{mn} = \sum_r Y_{m,n-r}^{(g)} V_{mr}$ by admittance $Y_{m,n-r}^{(g)}$. Transmission line approach can solve the surface wave problem in a similar way as the RCWA-LW approach. From a different perspective, it treats the grating structure as a transmission line equivalent network, and it is easier to calculate the reflection coefficient at each interface, e.g. $\rho_n = (Y_n^g - Y_n^s)/(Y_n^g + Y_n^s)$ at the grating-substrate interface [20].

2.1.5 Coupled Wave Theory

Coupled wave theory, proposed by Kogelnik [21], can be categorized as an approximation method because only the incident reference wave R and the outgoing signal wave S that obey the Bragg condition are considered while the other diffraction orders are neglected. This assumption limits the coupled wave theory to thick hologram gratings. The model is based on a set of two equations (the coupled wave equations) regarding S and R as $C_R R' + \alpha R = -j\kappa S$ and $C_S S'(\alpha + j\theta)S = -j\kappa R$, where κ is the coupling constant, which indicates the energy interchange between S and R . The solution to the coupled wave equations is in the general form $R = r_1 e^{\gamma z} + r_2 e^{-\gamma z}$ and $S = s_1 r_1 e^{\gamma z} + s_2 r_2 e^{-\gamma z}$. The diffraction efficiency of the volume grating can be determined as $\eta = (|C_S|SS^*)/C_R$.

2.1.6 Perturbation Method

As a type of approximation method, perturbation method is commonly used to analyze surface relief gratings with small perturbations whose relative permittivity can be written analytically. The field in the grating is first expressed in a plane wave expansion $E_y(x, z) = \sum_m \tilde{E}_m e^{j\beta_m z}$. The grating permittivity, expressed in a Fourier series, and the field expansion are substituted to the wave equation, resulting in a second-order differential equation in \tilde{E}_m whose solution is subject to the continuity of E_y and H_z at boundaries. The unperturbed case, e.g. uniform waveguide, is first determined by considering only the 0th-order term in the second-order differential equation, and then the calculated $\tilde{E}_m(0)$ and β_0

are used to approximate higher order terms. This process provides a first-order perturbation solution for \tilde{E}_m [22].

2.1.7 Coupled Mode Theory

Coupled mode theory, an essential perturbation approach, is useful for treating problems involving energy exchange between modes, e.g. grating diffraction, evanescent coupling, electrooptic modulation, photoelastic and magnetooptic modulation, and optical filtering, etc. This theory essentially solves the coupled equations for two electromagnetic modes $a(z, x, t) = Ae^{j(\omega_a t \pm \beta_a z)} f_a(x)$ and $b(z, x, t) = Be^{j(\omega_b t \pm \beta_b z)} f_b(x)$ under perturbation, where the complex amplitudes A and B vary according to the coupled mode equations $\frac{dA}{dz} = \kappa_{ab}Be^{-j\Delta z}$, and $\frac{dB}{dz} = \kappa_{ba}Ae^{+j\Delta z}$, where Δ is the phase-mismatch constant, and κ is the coupling coefficient [23]. The solutions to the coupled mode equations depend on the power conservation condition, mode propagation directions, and boundary conditions.

2.1.8 Commercial PDE Solver

With simple user interfaces, commercial software packages such as Lumerical FDTD (finite-difference time-domain), COMSOL multiphysics (finite element method, FEM), or CAMFR (CAvity Modelling FRamework, eigenmode expansion) are popular tools to simulate grating structures. FDTD and FEM are based on the second type differential method, while CAMFR is based on the first type. However, using these tools to solve diffraction problems are typically very time-consuming. FDTD discretizes the problem in space and time, and it generally requires more computation points (higher resolution) to properly simulate a complicated structure in 3D, which greatly increases computational time. FEM requires the generation of connected meshes and nodal matrices which will be problematic when treating and updating large and complex geometries. What's more, FEM heavily relies on numerical integration which is a typically slow calculation process. CAMFR treats the field as a sum of local eigenmodes in each z-invariant layer. It approximates grating layer

as uniform dielectric layer, and thus it is challenging to simulate complex structures which require large number of modes.

2.2 Optimization solver

Optimization is a critical step to design efficient waveguide grating couplers. Optimization algorithms, such as genetic algorithms, trust regions method, interior point method, and gradient descent method, etc., need to be used in addition to the grating theories. The optimization algorithms take grating parameters (e.g. period, grating depth, fill factor and diffraction angle, etc.) as variables to optimize the target parameter (diffraction efficiency calculated by grating theories). This process involves multiple iterations and comparisons which greatly increase computation loads. As a result, an accurate and efficient grating theory, such as RCWA, is helpful in speeding up the optimization.

2.3 Waveguide Grating Coupler Design

Based on the theoretical studies, many waveguide grating structures have been proposed to increase the coupling efficiency. The most effective approaches have been choosing materials with large refractive index contrast (e.g. SOI) and optimizing the grating period, etch depth, and fill factor [24], which fundamentally change the diffraction behavior. However, further efficiency improvement into the desired diffraction direction continues to be a challenge due to the presence of substrate leakage loss, back-reflection, and forward-transmission (Fig. 2.1). These problems have been mitigated by applying poly-Si overlays (to enhance directionality) [25], asymmetric profiles (to enhance directionality) [26], DBR or metal reflectors (to reduce substrate leakage) [27], apodized or chirped gratings (to reduce back-reflection) [28], in-plane grating reflectors (to reduce forward-transmission) [29], dual-grating layer [30], and novel subwavelength structures [31, 32]. Focusing gratings [33], whose grating rulings are curved, are also proposed to counteract the spreading of the diffracted fields. Some reported SOI gratings are summarized in Table 2.1.

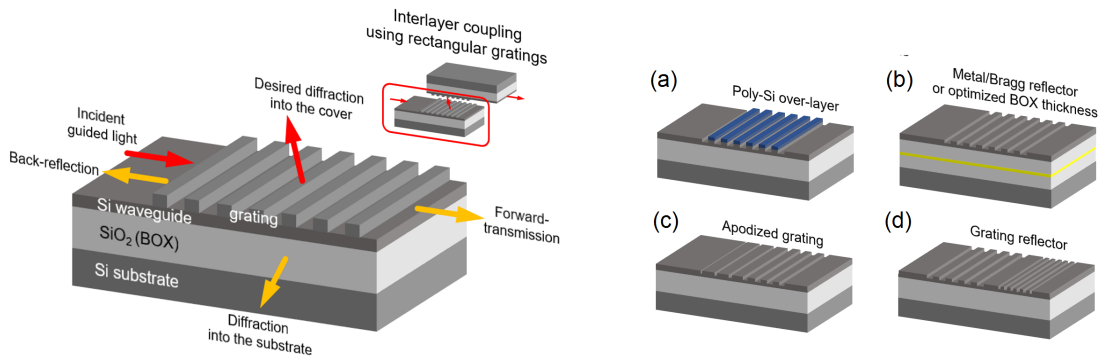


Figure 2.1: Optical losses present in rectangular gratings used for interlayer coupling. Possible solutions to reduce losses in a binary SOI grating out-coupler are (a)(b) increasing directionality to cover, (c) reducing back-reflection, and (d) reducing forward-transmission.

Table 2.1: Some reported SOI gratings for TE polarization. The column labels represent Si waveguide thickness (t_{Si}), grating period (Λ), grating etch depth (t_g), grating fill factor (f), grating line resolution (δ), grating length or dimension (L), single-grating efficiency (η_s), working wavelength (λ), and 1dB or 3dB bandwidth (1dB/3dB). CP, AP and DE represent chirped grating period, apodized fill factor, and double etch depths/widths, respectively.

t_{Si} (nm)	Λ (nm)	SOI Structure			Measurement			Simulation			Reference and Comments	
		t_g (nm)	f	δ (nm)	L (μm)	η_s (%/dB)	λ (nm)	1dB/3dB (nm)	η_s (%/dB)	λ (nm)	1dB/3dB (nm)	
220	CP	220	AP	120	11	35/-4.6	1536	47/-	72/-1.4	1550	38/-	1 ^a
250	CP	—	AP	60	14	64/-1.9	1524	42/70	74/-1.3	1520	50/80	2 ^a
220	640	70	0.5	320	12.8	91/-0.41 ^b	1590	—	94/-0.28 ^b	1550	—	3 ^c
220	630	70	0.5	315	15.75	69.5/-1.6	1520	36/63	76/-1.2	1550	40/60	4 ^d
220	CP	100	AP	30	13	—	—	—	88/-0.6	1550	—/40	5 ^d
220	630	70	0.5	315	—	—	—	—	79/-1.0	1550	—	6 ^d
220	610	70	0.5	305	12.2	55/-2.6	1530	50/-	66/-1.8	1550	55/-	7 ^e
340	630	340	0.85	95	10	44/-3.6	1560	—/50	—	—	—	8
340	CP	200	AP	43	15	75.8/-1.2	1533	—/45	79/-1.0	1550	—/48	9
220	701	220	0.5	350	14	—	—	—	49/-3.1	1550	20/35	10
220	568	DE	AP	100	—	65/-1.9	1310	23/-	85/-0.7	1310	25/-	11 ^f
220	780	DE	DE	100	30	74/-1.3	1550	—/52	78/-1.1	1550	—/50	12 ^f
220	663	DE	AP	87	15	71/-1.5	1533	—/49	87/-0.6	1550	—/50	13 ^f
510	545	350	AP	—	—	—	—	—	81/-0.9	1560	42/-	14 ^f
380	430	70	0.5	215	14	43/-3.7	1310	—	—	—	—	15
300	565	150	0.77	130	12.4	—	—	—	78/-1.1	1550	—/65	16 ^g
120	—	—	—	—	—	92/-0.36	1197	—	95/-0.2	1200	—/100	17 ^g
250	420	250	0.54	227	10	—	—	—	85.3/0.69	1310	—/20	18 ^h

^a Optimized BOX layer thickness

^b η_s approximated by $\sqrt{\eta_c}$

^c Gold reflector

^d Bragg reflector

^e Poly-Si overlay

^f Subwavelength structure

^g Dual-grating layer

^h In-plane reflector

¹ Opt. Express **19**, 3592 (2011)

² Opt. Lett. **35**, 1290 (2010)

³ Appl. Phys. Express **7**, 032202 (2014)

⁴ Conf. Lasers Electro-Optics (2009) p.CTuC6

⁵ Opt. Lett. **29**, 2749 (2004)

⁶ Jpn. J. Appl. Phys. **45**, 6071 (2006)

⁷ Appl. Phys. Lett. **92**, 131101 (2008)

⁸ Microelectron. Eng. **86**, 1114 (2009)

⁹ Photon. Technol. Lett. **22**, 1156 (2010)

¹⁰ Opt. Express **17**, 11066 (2009)

¹¹ Opt. Express **25**, 17864 (2017)

¹² Opt. Lett. **40**, 4190 (2015)

¹³ J. Lightwave Technol. **35**, 4663 (2017)

¹⁴ Opt. Commun. **355**, 161 (2015)

¹⁵ Opt. Lett. **28**, 1150 (2003)

¹⁶ Opt. Express **23**, 1691 (2015)

¹⁷ Optical Fiber Commun. Conf (2016) 1

¹⁸ Opt. Express **23**, 24433 (2015)

CHAPTER 3

RECTANGULAR GRATING COUPLER: EFFICIENCY OPTIMIZATION AND ANGULAR MISALIGNMENT ANALYSIS

Rigorous coupled-wave analysis is an accurate and efficient method to study the grating diffraction phenomena. However, its formulation relies on energy conservation in the plane normal direction, and thus RCWA doesn't provide the in-coupling/out-diffraction efficiencies of waveguide gratings in which surface waves (or leaky wave) are involved. The RCWA-leaky wave (LW) approach was proposed to investigate the out-diffraction process of thick volume gratings made of polymer [34], but it is tedious to implement and less practical for thin SOI gratings. RCWA-LW approach involves an intermediate step to determine a complex propagation constant $\tilde{\gamma} = \beta - j\alpha$, which is critical for the calculation of out-diffraction efficiencies. The parameter $\tilde{\gamma}$ is obtained such that the determinant of the boundary condition matrix is zero. This intermediate calculation is based on the Muller method, and careful choices of the initial guesses are crucial for the Muller method to converge to meaningful results, which is especially difficult to achieve for material systems with large-index differences (e.g. SOI gratings). This method also requires matrix inversion, which usually results in large numerical errors when the matrix is big and close to singular. In addition, RCWA-LW approach is insufficient to study the in-coupling process, so it can't adopt the useful formulations of 3D RCWA regarding the conical incidence.

In this chapter, a new concept, the “equivalent index slab (EIS)”, is proposed to determine the complex propagation constant $\tilde{\gamma}$, which circumvents the problem of solving the determinant of a large-dimension matrix. This extends the applicability of RCWA-EIS to arbitrary material systems. In conjunction with the Matlab built-in optimization tools, the RCWA-EIS method can be applied to optimize grating in-couplers as well as out-couplers due to light reciprocity. Since the RCWA-EIS formulations are based on the in-coupling

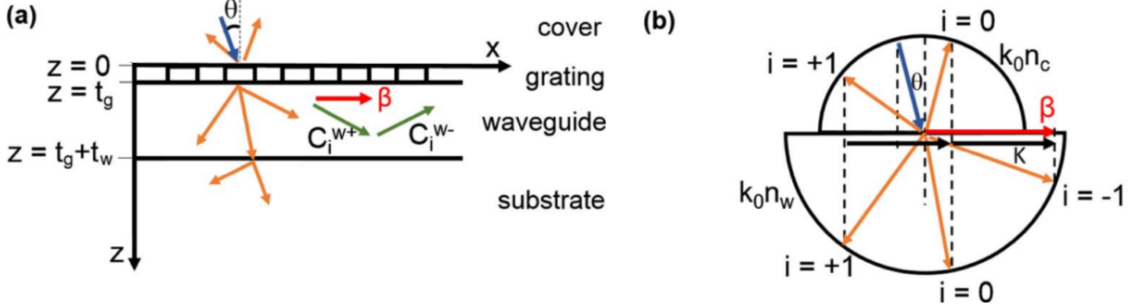


Figure 3.1: Schematic representation of (a) the grating in-coupling process and (b) the phase diagram based on the Floquet condition. This example shows multiple diffraction orders in the cover and substrate (not optimized for high efficiency), and the $i = -1$ order is a possible guided order whose propagation constant in the x direction is approximately equal to the guided mode propagation constant β in the waveguide.

process, conical incidence on the waveguide grating can be considered, which facilitates the analysis of angular misalignment effects on the interlayer grating coupling.

3.1 RCWA-EIS Method

The RCWA-EIS method starts with the formulations of the conventional RCWA [35]. A surface-relief grating in the TE polarization (E_y , H_x and H_z) is considered as an example. As shown in Fig. 3.1, the waveguide grating structure can be divided into four layers, namely cover, grating, waveguide, and substrate. A plane wave with free-space wavelength λ_0 is obliquely incident onto the grating at an angle θ .

3.1.1 Step 1: Calculate Fields using Conventional RCWA

The electric fields in all layers are expressed as plane wave expansions $E_y = \sum_i Z(z) e^{-jk_{x,i}x}$, where i indicates the i th diffraction order, $Z(z)$ is a function in the z direction containing unknown field amplitudes, and $k_{x,i} = k_0 n_c \sin \theta - iK$ is the propagation constant in the x direction. The magnetic fields H_x are derived according to the Maxwell's equation. The grating permittivity $\epsilon_g(x)$ is expressed in a Fourier series along the x direction, which is integrated into the wave equation to determine the electric field in the grating layer whose

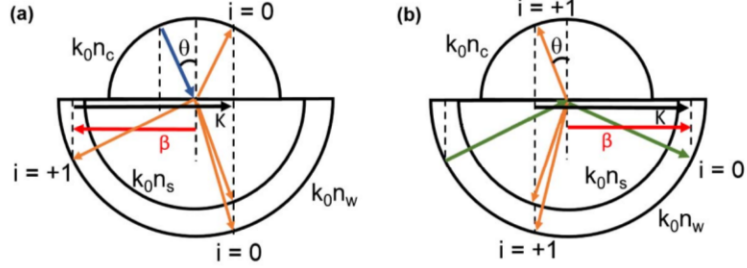


Figure 3.2: Phase diagram of (a) the grating in-coupling and (b) the out-diffraction process with only the 0th and 1st orders. The light in-coupling into the 1st order in (a) is the reciprocal process of the guided wave out-diffraction into the 1st order in (b).

$Z(z)$ component can be expressed in a matrix. The field amplitudes are solved by matching tangential fields at all interfaces. The derivations can be found in [24].

The in-coupling efficiency can't be directly calculated, since power flow in the x direction is not considered in the conventional RCWA. As a result, we need to take advantage of the light reciprocity and use the out-diffraction process to calculate the in-coupling diffraction efficiency in a similar way as in the RCWA-LW approach. A complex propagation constant $\tilde{\gamma} = \beta - j\alpha$ needs to be defined. The grating is designed such that only the 0th and 1st orders are propagating in the cover and the substrate when light is incident from the cover, which ensures the minimum number of propagating orders and thus maximizes diffraction efficiencies. The 1st order diffracted wave is coupled into the waveguide, as shown in Fig. 3.2. All fields in the structure, as well as the propagation constant β , can be determined from the in-coupling process analyzed by the conventional RCWA. By reciprocity, in-coupled light and out-diffracted light should have the same real propagation constant β in the x direction. The problem becomes finding the radiation factor α that will be used to calculate the diffraction efficiencies.

3.1.2 Step 2: Define Equivalent Index Slabs

The grating layer, whose field expansion involves a sum of exponential terms, is replaced by L layers of uniform equivalent slabs with unknown refractive indices, and the i th order

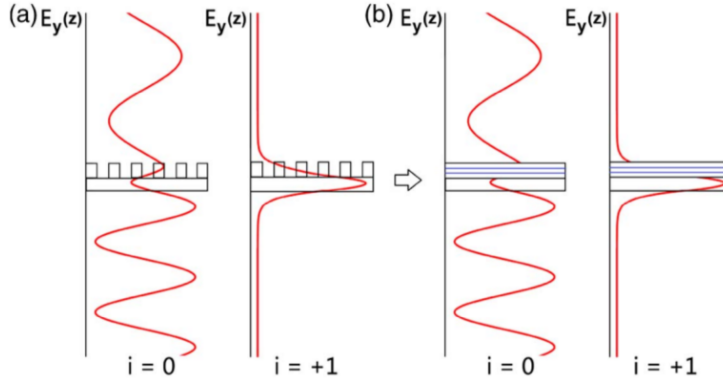


Figure 3.3: Schematic representation of field repetition outside of the grating by equivalent index slabs. (a) Electric field amplitude along the z direction of the multilayer grating structure, and (b) equivalent index slabs are used to replace the grating layer. It is not necessary to consider the fields inside the grating region.

electric field in the z direction of the l th slab $Z_{ly,i}(z)$ is expressed in the same mathematical form as the one for the waveguide $Z_{ly,i}(z) = C_i^{l+} e^{-jk_{lz,i}[z-(l-1)t_l]} + C_i^{l-} e^{jk_{lz,i}(z-lt_l)}$, where $t_l = t_g/L$, t_g is the grating height, and the parameter L is chosen to be 4 which will be explained later. With only two propagating diffraction orders ($i = 0$ and 1) involved, the only requirement for the definition of the equivalent slabs is keeping the field amplitudes and phases of the 0th and 1st orders at the cover-grating interface and at the grating-waveguide interface the same as calculated using conventional RCWA. As shown in Fig. 3.3, the equivalent slabs generate the same fields outside grating region, which is the deterministic step because the radiation losses are mainly due to the radiation in the cover and the substrate. Similar to a black box, the complicated field expansion inside of the box is replaced by simple expressions, while the outside fields remain unchanged.

By imposing boundary conditions on the electric and magnetic fields, transfer matrix formulations can be constructed and a total of four equations related to the E_y fields and H_x fields of each of the 0th order and 1st order are obtained. The number of unknown variables (the refractive indices of the equivalent slabs) involved in the four equations is L . By choosing $L = 4$, the number of unknown equals the number of equations, which allows the use of the trust-region-dogleg algorithm of the *fsolve* solver in Matlab [26]. Then the

unknown refractive indices of the equivalent slabs can be readily solved.

3.1.3 Step 3: Calculate Radiation Factor

After the refractive indices of equivalent slabs are determined, the radiation factor α is determined using a similar process as that discussed in [36]. But here, we will consider two out-diffracted orders with $k_{x,0} = \beta - j\alpha$ and $k_{x,1} = K - \beta - j\alpha$ as propagation constants in the x direction. The transfer matrix formulations for both orders are in the forms as in Step 2 except that all layers, including cover, equivalent index slabs, waveguide and substrate, are all considered. This results in two equations with one unknown (α), which can be solved using the Levenberg-Marquardt algorithm in *fsolve*. The matrix dimension treated here (2×2) is much smaller than that used in RCWA-LW approach ($6N \times 6N$), where N is the total number of diffraction orders, which avoid the problematic step of solving the determinant in the RCWA-LW approach. Step 2 and 3, which manifest the EIS concept, eliminate the less important evanescent orders considered in RCWA-LW approach when calculating the radiation factor, thus greatly improving the calculation efficiency and numerical stability.

3.1.4 Step 4: Calculate Out-Diffraction Efficiency

After the radiation factor α is determined, the out-diffraction efficiency, equivalently in-coupling efficiency, can be calculated by substituting the complex propagation constant $\tilde{\gamma} = \beta - j\alpha$ into the homogeneous system of equations, $\mathbf{M}\mathbf{x} = \mathbf{0}$, used in RCWA-LW approach [24]. The field coefficient vector \mathbf{x} can be solved using the singular value decomposition of the matrix \mathbf{M} , which is $\mathbf{M} = \mathbf{U}\mathbf{S}\mathbf{V}^T$. The solution \mathbf{x} is the column vector of \mathbf{V} corresponding to the smallest singular value. Then the efficiencies into the cover and substrate DE , which are the out-diffraction efficiencies, can be solved in the conventional way as $DE = PC(1 - e^{-2\alpha l})$, where PC is the preferential coupling ratio and l is the grating length [24].

3.2 Efficiency Optimization

3.2.1 Optimization Procedures

The grating coupler is optimized using the Matlab optimization solver *fmincon* together with the RCWA-EIS method. The RCWA-EIS method determines the in-coupling/out-diffraction efficiencies DE of the grating coupler in a specific configuration (e.g. given grating profile, diffraction angle θ , grating height t_g , grating period Λ , fill factor f , etc.), and the solver *fmincon* minimizes the target function $(1 - DE)$ by varying the grating parameters according to a set of constraints. The 1st order out-diffraction efficiency $DE_{c,1}$, equivalently the 1st order in-coupling efficiency (Fig. 3.2), determined by the RCWA-EIS method is the target to optimize in the solver *fmincon*. Since the grating is designed to couple the 1st order diffracted wave into the waveguide, $k_{x,1}$ should be comparable to the fundamental propagation constant of the slab waveguide β_0 , which can be calculated using the method introduced in [36]. In the optimization, $k_{x,1}$ is restricted to be in the range $|\beta_0 - k_{x,1}| < k_0 n_w - \beta_0$. The inputs to the optimization solver *fmincon* are as follows: (1) the initial values of a set of undecided parameters, e.g., incident angle (or coupling angle) θ , fill factor f , grating period Λ , grating thickness t_g , etc, (2) the lower and upper bounds of each parameter, (3) the function tolerance, and (4) the constraint $|\beta_0 - k_{x,1}| < k_0 n_w - \beta_0$. The model outputs the final values of those parameters that give the minimum value of $1 - DE_{c,1}$, which corresponds to maximizing $DE_{c,1}$. The optimized structure can be validated by 2D FDTD simulation (e.g. MEEP program developed at Massachusetts Institute of Technology). Multiple runs with different sets of initial values can be conducted in order for the solver to find the global minimum.

3.2.2 Results and Discussion

Four types of grating structures, namely binary gratings, parallelogramic gratings, sawtooth gratings, and volume gratings, are analyzed to demonstrate the flexibility of the model. For

the three types of surface-relief gratings, coupling angle θ , grating period Λ , and grating thickness t_g are the unknowns to be optimized. The other parameters are as follows: free-space wavelength $\lambda_0 = 1.55 \mu m$, cover, waveguide, substrate, grating groove, grating ridge indices $n_c = 1$, $n_w = 3.45$, $n_s = 1.45$, $n_{gr} = 1$, $n_{rd} = 2.46$, fill factor $f = 0.5$, and waveguide thickness $t_w = 0.22 \mu m$. The optimal slant angle of the parallelogramic grating can be calculated once the grating period is determined [26]. The volume grating considered here has sinusoidally-modulated permittivity within the waveguide. Coupling angle θ , grating period Λ , and slant angle ϕ are unknowns to be optimized. The other parameters are as follows: $\lambda_0 = 1.55 \mu m$, $n_c = 1$, $n_w = 1.8$, $n_s = 1.45$, $t_w = 0.4 \mu m$, $t_g = 0.4 \mu m$, average grating index $n_g = 1.8$, and index modulation $\Delta n_g = 0.1$. The in-coupling/out-diffraction efficiencies ($DE_{c,1}$) as a function of number of grating periods (N) of selected optimized gratings are shown in Fig. 3.4. Corresponding optimized values are summarized in Table 3.1. The results obtained from the RCWA-EIS match well those calculated by the FDTD.

The fundamental mode propagation constant of the $0.22 \mu m$ thick waveguide for the surface-relief gratings is calculated to be $\beta_0 = 11.3710 \mu m^{-1}$, while that of the $0.4 \mu m$ thick waveguide for the volume gratings is calculated to be $\beta_0 = 6.3008 \mu m^{-1}$. The propagating constants β shown in Table 3.1 are comparable to the corresponding β_0 . Binary gratings, e.g. case (a), radiate the incident power (or guided power) almost equally into the cover and the substrate, resulting in a preferential coupling ratio (or radiation directionality) close to 0.5 (e.g. $PC_{c,1} = 0.4914$) provided the refractive index of the cover is comparable to that of the substrate. Parallelogramic gratings, e.g. case (b), demonstrate the highest efficiency

Table 3.1: Optimized parameters and calculated in-coupling/out-diffraction efficiencies for selected cases of binary gratings, parallelogramic gratings, sawtooth gratings, and the volume gratings. $PC_{c,1}$ is the preferential coupling ratio, defined as the fraction of the total radiation power that is diffracted into the +1 order in the cover.

Case No.	Initial Values				Optimized Values							
	θ (rad)	Λ (μm)	t_g (μm)	ϕ (rad)	θ (rad)	Λ (μm)	t_g (μm)	ϕ (rad)	$PC_{c,1}$	$DE_{c,1}$ @ N=50	β (μm^{-1})	α (μm^{-1})
(a)	0.30	0.60	0.10	–	0.30	0.60	0.23	–	0.4914	0.4392	9.2742	0.0375
(b)	0.10	0.55	0.30	–	0.24	0.55	0.30	0.9831	0.8005	0.7177	10.4801	0.0412
(c)	0.10	0.55	0.20	–	0.37	0.50	0.34	–	0.8925	0.3214	11.0561	0.0089
(d)	0.30	0.70	–	1.2	0.10	0.70	–	0.9255	0.5968	0.3010	6.7298	0.0098

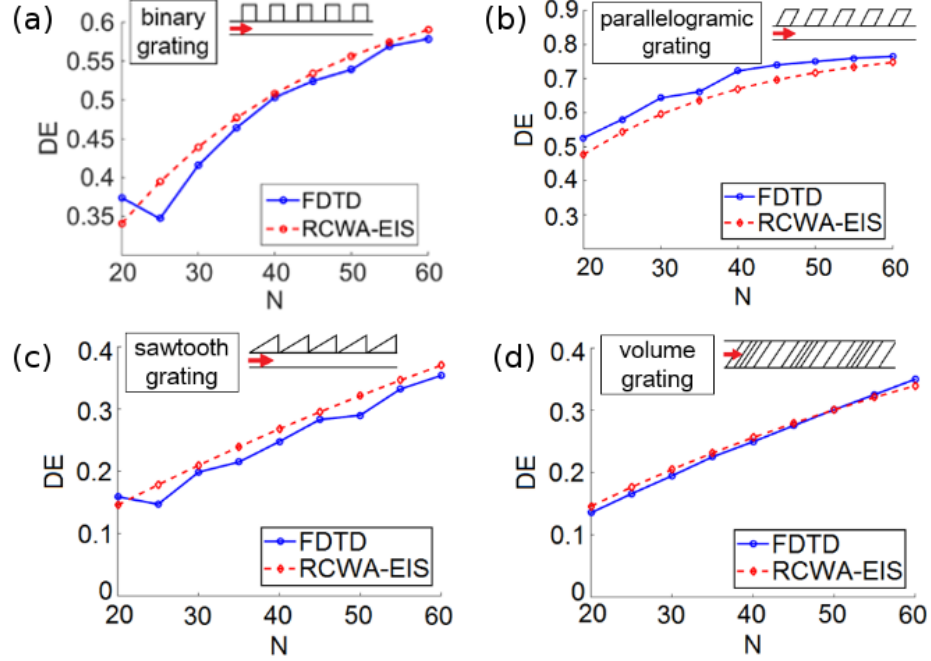


Figure 3.4: In-coupling/out-diffraction efficiencies ($DE_{c,1}$) as a function of number of grating periods (N) for selected cases of optimized binary gratings, parallelogrammatic gratings, sawtooth gratings, and the volume gratings.

into the cover due to their large radiation factor (e.g. $\alpha = 0.0412 \mu\text{m}^{-1}$) and asymmetric grating profile (e.g. $PC_{c,1} = 0.8005$). Sawtooth gratings, e.g. case (c), is not efficient because of their small radiation factor (e.g. $\alpha = 0.0089 \mu\text{m}^{-1}$), even though their asymmetric profile can enhance the directionality into the cover (e.g. $PC_{c,1} = 0.8925$). For volume gratings, the diffraction efficiency is relatively small due to the small index modulation Δn_g . Since the majority of the volume gratings are made of polymer with typical indices from 1.3 to 1.7, and the index modulation Δn_g is usually less than 0.1, the diffraction efficiency of the volume gratings should not be compared with those of surface-relief gratings with large index differences.

Surface-relief gratings with bottom reflectors can also be optimized using the RCWA-EIS method. Gratings with symmetric profiles have approximately half of the out-diffracted power travelling into the substrate, and thus it is beneficial to recycle the downward-diffracted light using an adjacent-layer reflector. Two types of reflectors are considered, namely grating reflectors and metal reflectors. The RCWA-EIS formulation remains the

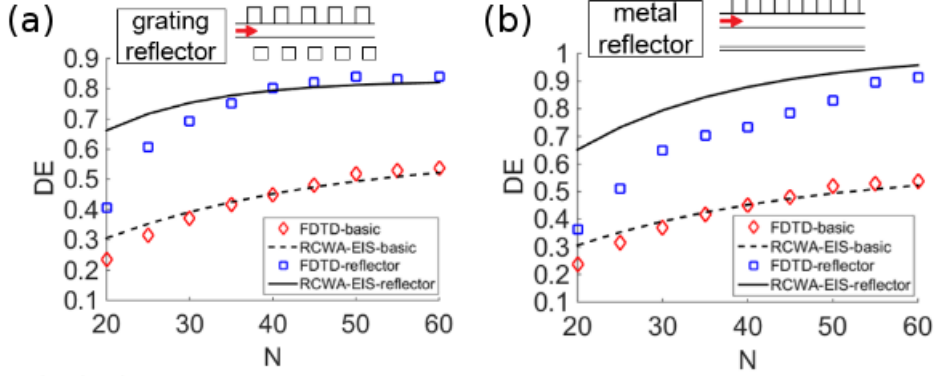


Figure 3.5: In-coupling/out-diffraction efficiencies ($DE_{c,1}$) as a function of number of grating periods (N) for optimized binary gratings with bottom grating reflector and metal reflector. Applying reflector results in twofold increase in diffraction efficiencies.

same except for the addition of more layers corresponding to the reflectors. The grating reflector is replaced by equivalent index slabs, while the metal layer is treated as a uniform layer with negative real and positive imaginary relative permittivity, e.g. for gold, $\epsilon_r = 112.68+j6.852$ at $1.55 \mu m$ wavelength. The reflectors are added to several optimized binary gratings. To optimize the reflector structure, three parameters, namely the buried oxide layer (BOX) thickness (d), grating reflector thickness (t_{bg}), and the horizontal shift of the grating reflector relative to the optimized binary grating (Δ_x), are set as unknowns for the case of grating reflector, whereas two parameters, namely the BOX thickness (d) and metal layer thickness (t_m), are set as unknowns for the case of metal reflector.

An optimized binary grating with parameters $t_g = 0.27 \mu m$, $\Lambda = 0.67 \mu m$, and $\theta = 0.10 rad$ is used as the basic structure to which reflectors can be applied. Optimized parameters found for the grating reflector are $\Lambda_{bg} = \Lambda = 0.67 \mu m$, $t_{bg} = 0.31 \mu m$, $d = 0.22 \mu m$, and $\Delta x = 0.30 \mu m$, while those for the metal reflector are $t_m = 0.51 \mu m$, and $d = 1.02 \mu m$. Figure 3.5 shows the in-coupling/out-diffraction efficiency ($DE_{c,1}$) as a function of the number of grating periods (N) for the basic grating with/without the reflectors. From RCWA-EIS results, applying the grating reflector results in twofold increase in diffraction efficiencies. Mismatch in FDTD and RCWA-EIS data is due to the geometric issue that RCWA assumes infinite long gratings, while FDTD simulates gratings with real lengths.

In conclusion, the RCWA-EIS method together with the Matlab optimization solver *fmincon* can be used to optimize grating couplers with various profiles. The advantages of this optimization method are arbitrary choices of grating profiles, wide parameter search spaces, easy implementation, fast calculation, and accurate results.

3.3 Angular Misalignment Analysis

Alignment of diffraction gratings has been a major bottleneck that limits the interlayer grating coupling efficiency. The need to align the grating couplers and other optical components greatly reduces the possibility of cost-effective manufacturing and automation. Misalignment may result from mechanical and thermal effects which are unavoidable during device handling and operation. As a result, understanding the underlying mechanism and designing misalignment-tolerant grating couplers are important to the fields of packaging and testing.

There are six degrees of freedom to be considered for misalignment analysis, including three lateral (x, y, z) and three angular (roll, pitch, yaw), where roll, pitch, and yaw are the rotational angles about the x, y , and z axes, respectively. For chip-to-chip grating couplers, the lateral displacements of volume holographic gratings [37] and surface-relief gratings [38] have been experimentally studied. There is limited effort analyzing rotational misalignment, and such efforts all focus on rotations about the y -axis, or equivalently, changes in the incident angle [39]. This work, for the first time, calculate interlayer grating coupling efficiency for an arbitrary rotation using the 3D RCWA for conical diffraction together with the RCWA-EIS method [40]. The model is computationally efficient and numerically accurate, compared with 3D FDTD simulations which require hefty simulation time. For example, it generally requires 3 days to finish one 3D FDTD simulation at a resolution of 60 pixels per unit distance with 20-core parallel computing, and it would take even longer when the resolution is set to a higher value. In comparison, it takes only 0.3 second for the RCWA-EIS method to calculate the efficiency of a rotated grating.

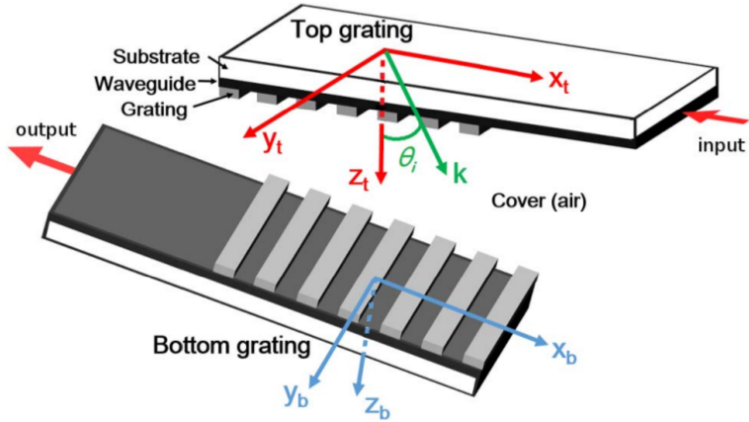


Figure 3.6: Schematic representation (not to scale) of the 3D interlayer grating coupling configuration under angular misalignment.

3.3.1 Analysis Procedures

The general 3D interlayer grating coupling configuration is depicted in Fig. 3.6. The bottom grating is rotated relative to the top grating. A guided wave is launched into the top waveguide along the $-x_t$ direction and out-diffracted from the top grating, and the out-diffracted light is then incident conically onto the bottom grating. Assume the gratings are optimized for high diffraction efficiencies and only two orders (0th and 1st) are propagating in the cover. The analysis begins with determining the conical incidence configuration (proper Euler angles) from the relative rotation of the bottom grating. Then the conical incidence can be analyzed using the traditional 3D RCWA formulations, and the field amplitudes and phases at all interfaces can be determined. The equivalent index slabs can be subsequently defined and coupling efficiency into the waveguide can be calculated.

3.3.2 Results and Discussion

An optimized binary grating with parameters $t_g = 0.32 \mu m$, $\Lambda = 0.65 \mu m$, and $\theta = 0.20 rad$ is used for the angular misalignment analysis. For demonstration, the bottom grating is rotated about the x axis, the z axis, and the vector [2 2 1]. Figure 3.7 shows the

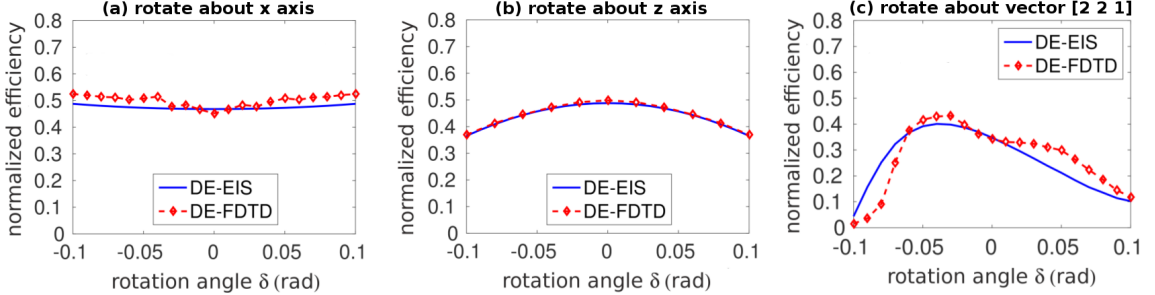


Figure 3.7: Bottom grating in-coupling efficiency as a function of rotation angle. For (a) and (b), $N = 50$; for (c), $N = 30$ (shorter grating due to geometric constrain under rotation).

bottom grating in-coupling efficiency DE_b as a function of rotation angle (δ , with respect to coordinate rotations) for the three rotation schemes. Rotations about the x and z axis have less effect on DE_b than rotation about [2 2 1]. This is because the vector [2 2 1] has a relatively large y component. Rotation about the groove direction (y axis) produces the largest deviation from the Bragg condition and DE_b is correspondingly reduced. As a result, system designers should try to align the grating such that there is minimal rotation about the y axis, e.g. rotation should be limited to $\pm 3^\circ$ to achieve less than 10% change in DE_b . As can be observed from Fig. 3.7(c), the efficiency versus rotation angle curve is asymmetric. On one hand, the rotation axis is not a principle axis and deviations from the Bragg condition may result in different efficiency changes. On the other hand, the slight efficiency increases at negative δ (coordinate system is rotated clockwise or equivalently the bottom grating is rotated counterclockwise) correspond to the configurations where the bottom grating is closer to the light-launching side of the top waveguide, and thus more power may be evanescent-coupled to the bottom waveguide. The effect of rotation about the the x axis or the z axis should be symmetric for positive and negative rotations. For rotation about the x axis, the efficiency increases about 5% at $\delta = \pm 0.1 \text{ rad}$, which may due to the over-modulation of gratings under off-Bragg conditions.

In summary, RCWA-EIS method has been extended to the conical diffraction cases and applied to the simulation of interlayer grating coupling efficiency under angular misalignment. The rectangular grating is found to be sensitive to angular misalignment.

CHAPTER 4

GRATING-ASSISTED-CYLINDRICAL-RESONANT-CAVITIES INTERLAYER COUPLER: THEORETICAL DESIGN AND EXPERIMENTAL VALIDATION

Rectangular diffraction gratings have been popular candidates to achieve interlayer optical coupling. However, many challenges still exist which hinder rectangular gratings from serving as efficient couplers. For SOI gratings, narrow grating ridges ($\sim 100\text{ nm}$) are required to achieve relatively high efficiency ($>70\%$, see Table 2.1), and such gratings can only be patterned using high-cost fabrication techniques, e.g. e-beam lithography. The methods used to increase the directionality, e.g. depositing overlayers or applying reflectors, also add complexity to the fabrication process. Apart from the fabrication difficulties, grating assembly poses additional challenges to photonics integrations because rectangular grating couplers are sensitive to misalignments. All of these issues originate from the Floquet and Bragg conditions which rectangular gratings must inherently follow.

In this work, a fundamentally different approach, the grating-assisted-cylindrical-resonant-cavities (GARC) interlayer coupler [41], is proposed to achieve efficient interlayer optical coupling. The coupler consists of a pair of circular gratings with a high-index via. The via plays a significant role as a cylindrical resonant cavity in the vertical direction, and the GARC coupler thus benefits from the wavelength selectivity and the large increase of the resonant optical field introduced by the cavity. In addition, the outer circular gratings serve as distributed Bragg reflectors, forming another set of resonant cavities in the horizontal direction and enhancing the fields which are modulated by the inner circular gratings. Since the GARC coupler exploits the constructive interference and evanescent coupling instead of following the Floquet condition of rectangular gratings, relatively wide grating ridges can be used and there is no need to incorporate adjacent-layer reflectors, thus reducing the fabrication cost. At $1.55\text{ }\mu\text{m}$ wavelength, the simulated coupling efficiency obtained from

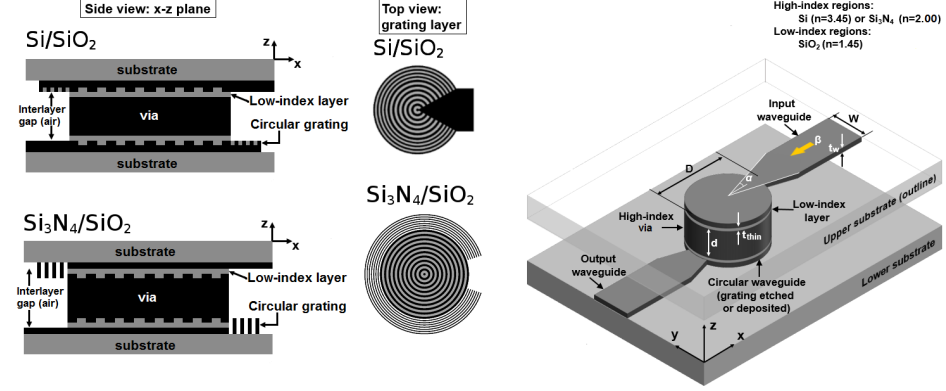


Figure 4.1: Schematic representation of the GARC interlayer coupler. Two types of GARC structures determined by material systems (Si/SiO_2 and $\text{Si}_3\text{N}_4/\text{SiO}_2$) are shown.

an optimized Si/SiO_2 GARC coupler (71% or -1.5 dB interlayer coupling efficiency) are relatively high compared with those obtained from the conventional SOI rectangular gratings (Table 2.1). Perhaps the most significant benefit of GARC coupler is the wide spectral bandwidth, which can't be achieved by conventional rectangular gratings. The GARC couplers also demonstrate many advantages such as CMOS compatible fabrication, flexible choices of interlayer separation, and high misalignment tolerances.

4.1 Theoretical Design

Figure 4.1 shows the GARC coupler in which relatively high-index waveguides and a via are configured to couple optical signals between layers separated by an air gap. This structure can be implemented between two separate overlaid chips or embedded within an on-chip interconnect stack. In the second case, the air gap can be filled with SiO_2 , which will cause only small changes to the overall design. Transverse electric (TE, H_z , H_r , H_θ , E_r , E_θ) polarization is considered for demonstration.

4.1.1 GARC Coupler Model

For the TE polarization, the E_θ field in the circular slab waveguide is of primary importance because it is tangent to the cylindrical wavefront. The E_θ field is expressed in cylindrical

coordinates as [41]

$$E_\theta = \frac{j\omega\mu_0}{\beta^2} \sum_{\nu=-\infty}^{\infty} C_\nu \frac{d[J_\nu(\beta r)]}{dr} \cos(\gamma z) e^{j\nu\theta}, \quad (4.1)$$

where ν is the cylindrical mode order, J_ν is the ν -th order Bessel function representing a radial standing wave, β is the radial (r) propagation constant, and γ is the longitudinal (z) propagation constant. The guided-mode wavelength λ_ν of the ν -th mode is determined as the difference between two consecutive zeros of the function $d[J_\nu(\beta r)]/dr$.

When the circular grating is present, the guided mode in the circular waveguide will be perturbed but β will not be affected, which differs from the case of a rectangular grating whose h -th order horizontal propagation constants β_h are modified by the grating vector magnitude K through the Floquet condition $\beta_h = \beta_0 - hK$. This is because the radial fields in the circular region, represented by $J_\nu(\beta r)$, are not periodic. Since β is larger than the propagation constant k_{clad} , the longitudinal field in the cladding is evanescent. Therefore, a high-index via needs to be incorporated between the two circular gratings to provide an optical path for vertical coupling. The evanescent behavior in the cladding makes it unnecessary to incorporate reflectors because all the propagating light will be concentrated in the high-index via.

The circular grating can be divided into two regions. The inner region is designed for field perturbation, and the outer region serves as an in-plane circular distributed Bragg reflector. The inner grating periods Λ_i , inner ridge widths w_i , outer grating periods Λ_o , and outer ridge widths w_o are expressed based on interference conditions as [41]

$$\Lambda_i = p\lambda_\nu, \quad w_i = \frac{p}{2}\lambda_\nu, \quad \Lambda_o = \frac{s}{2}\lambda_\nu, \quad w_o = \frac{2t-1}{4}\lambda_\nu, \quad (4.2)$$

where p , s and t are arbitrary integers, and thus the grating ridges can be relatively wide provided the interference conditions are satisfied. The cylindrical mode order $\nu = 1$ is chosen to establish λ_ν because of its 180° rotational symmetry.

The stacking sequence of the GARC coupler is determined by the materials used. When the high-index regions (darker regions in Fig. 4.1) are made of Si, the grating is etched into the Si circular waveguide and filled with SiO₂. The low-index layer, made of SiO₂, is sandwiched between the grating and the via. Whereas in the Si₃N₄/SiO₂ GARC coupler, the grating is etched into the via and the low-index layer is located between the waveguide and the grating. This is because that the longitudinal field of the Si/SiO₂ waveguide is more confined in the waveguide core due to a larger refractive index difference. In order to effectively perturb the field in the circular waveguide, the grating needs to be etched into the waveguide. The etch depth should be shallow to reduce back-reflection into the input taper. By contrast, the longitudinal field extends further out of the waveguide core of the Si₃N₄/SiO₂ waveguide, and thus a grating layer adjacent to the waveguide is sufficient to perturb the field, while an etched grating may induce too much back-reflection.

4.1.2 Simulation Results

Figure 4.2 shows the cross-sectional views of the optimized Si/SiO₂ and Si₃N₄/SiO₂ GARC couplers. The parameters indicated in Fig. 4.1 for the optimized GARC couplers are summarized in Table 4.1. Full-wave simulations were performed using MEEP 3D FDTD. The Si/SiO₂ GARC coupler has a higher coupling efficiency ($\eta_c = 71\%$) than the Si₃N₄/SiO₂ GARC coupler ($\eta_c = 41\%$) due to a larger index difference and a stronger field confinement in the cavity. The circular grating ridges are defined according to the interference conditions Eq.(4.2) using different sets of parameters p , s and t , such that the minimum w_i of the Si/SiO₂ GARC coupler is 553 nm and that of the Si₃N₄/SiO₂ is 465 nm. Both GARC couplers exhibit wide spectral responses, e.g. 270 nm and 400 nm 1dB bandwidth for

Table 4.1: Parameter values for the optimized Si/SiO₂ and Si₃N₄/SiO₂ GARC couplers.

Case	β (μm^{-1})	n_{high}	t_w (μm)	t_g (μm)	t_{thin} (μm)	D_{in} (μm)	D_{out} (μm)	W (μm)	α ($^{\circ}$)	d (μm)	p	s	t	η_c (%)
Si/SiO ₂	11.37	3.45	0.22	0.04	0.1	14.08	20.72	10	28.65	2	2	3	2	71
Si ₃ N ₄ /SiO ₂	6.76	2	0.34	0.34	0.1	19.28	25.79	10	20	4.7	1	1	1	41

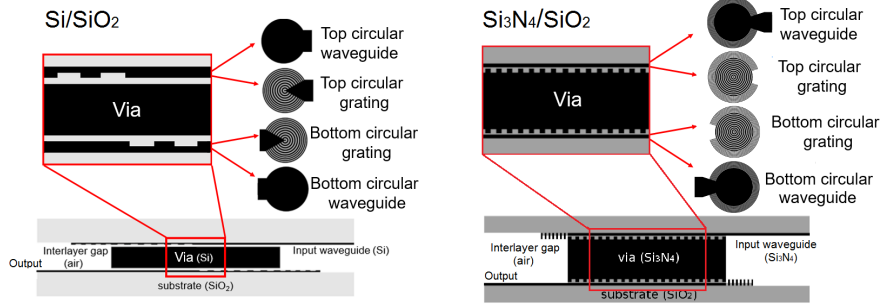


Figure 4.2: Cross-sectional views of the optimized Si/SiO₂ and Si₃N₄/SiO₂ GARC couplers.

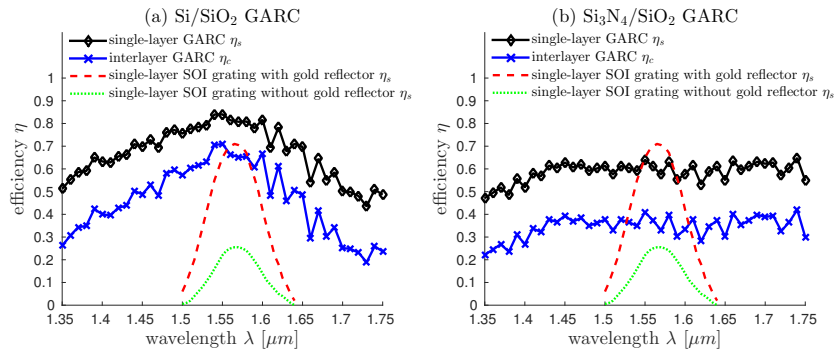


Figure 4.3: Spectral response for the optimized Si/SiO₂ and Si₃N₄/SiO₂ GARC couplers as well as that for the rectangular grating reported in [42].

Si/SiO₂ and Si₃N₄/SiO₂ GARC coupler respectively, as shown in Fig. 4.3.

The interlayer separation d , or the via height, is not limited to the optimized value in Table 4.1. Other optimal values are also possible provided the relation of d and the via radius R satisfies [43]

$$\lambda_{lm} = \frac{2\pi}{\sqrt{\left(\frac{\omega_l}{R}\right)^2 + \left(\frac{m\pi}{d}\right)^2}}, \quad (4.3)$$

where l and m indicate the resonant mode order in the radial (r) and longitudinal (z) directions, respectively, and ω_l is the l th zero of the function $J'_1(x)$. Take the Si/SiO₂ GARC coupler as an example. Since the GARC coupler is designed for the free-space wavelength $\lambda_0 = 1.55 \mu m$, the resonance wavelength in the Si via is $\lambda_{lm} = \lambda_0/n_{Si}$, which can be achieved using various sets of l , m , and d . The via height d at the (l,m) -th resonance can be found from Eq. (4.3), and some results are shown in Table 4.2. Since the radius of

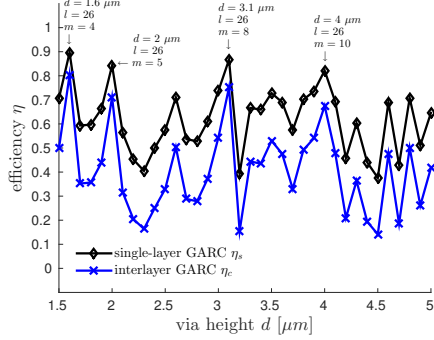


Figure 4.4: Plot of efficiency as a function of via height for the Si/SiO₂ GARC coupler.

$m \backslash l$	24	25	26	27	28
4	1.3801	1.4682	1.5807	1.7302	1.9413
5	1.7251	1.8353	1.9758	2.1627	2.4266
6	2.0701	2.2023	2.3710	2.5952	2.9119
7	2.4151	2.5694	2.7662	3.0278	3.3972
8	2.7602	2.9364	3.1613	3.4603	3.8825
9	3.1052	3.3035	3.5565	3.8929	4.3678
10	3.4502	3.6705	3.9516	4.3254	4.8531

Table 4.2: Via height d in μm for the (l,m) -th resonance at $1.55 \mu\text{m}$ free-space wavelength ($R = 7.0413 \mu\text{m}$) for the Si/SiO₂ GARC.

the cylindrical cavity is fixed at $R = 7.0413 \mu\text{m}$, the resonance mode order l in the radial direction can be approximated using $R = l\lambda_r/2$, where $\lambda_r = 2\pi/\beta = 0.5526 \mu\text{m}$ is the radial component of λ_{lm} . Thus l is approximated as 26, which results in the most prominent resonances in the cavity. The highlighted d values in Table 4.2, which are calculated using $m = 26$, correspond to the peaks in Fig. 4.4, which shows the plot of the coupler efficiency η as a function of via height d . Even though the via heights $1.6 \mu\text{m}$ and $3.1 \mu\text{m}$ lead to higher coupling efficiency (80% and 75%, respectively), the via height $2 \mu\text{m}$ is chosen in consideration of fabrication feasibility and device performance. The case $d = 2 \mu\text{m}$ has a longer coupling time (1.32 ps , temporal bandwidth $\delta_t = 0.76 \text{ THz}$) than $d = 3.1 \mu\text{m}$ (0.83 ps , $\delta_t = 1.21 \text{ THz}$) due to a stronger resonance. Nevertheless, the GARC couplers would be fast enough to satisfy the terahertz communication requirements.

4.2 Experimental Validation

The Si/SiO₂ GARC coupler will be fabricated on a silicon-on-insulator (SOI) wafer based on the optimal design shown in Table 4.1. Rectangular gratings and waveguides will be fabricated together with the circular gratings in order to introduce and extract optical signals into and out of the GARC couplers. Rectangular gratings with Si₃N₄ overlayers are

designed to couple the fiber signals. The Si_3N_4 layer will enhance the rectangular grating coupling efficiency as well as serving as etch masks for subsequent Si etching.

4.2.1 Preliminary Results

The SOI wafer is first characterized using Woollam M2000 Elipsometer, which approximates the layer thicknesses and refractive indices based on Cauchy model. Figure 4.5 shows the Si device layer thickness (a) and buried oxide layer thickness (b), which are approximately 220 nm and $3 \mu\text{m}$, respectively. In order to optimize Si_3N_4 deposition, a bare Si wafer is used as the test substrate and the Si_3N_4 layer is grown on the Si wafer using low pressure chemical vapor deposition (LPCVD) in Tystar Nitride furnace. The processing temperature is 550°C and the deposition gases are N_2 , SiH_2Cl_2 (DSC), and NH_3 . The film thickness ($\sim 120 \text{ nm}$, Fig. 4.6) and refractive index (~ 2) are characterized by Woollam M2000 Elipsometer. Another important step in the fabrication is patterning the rectangular and circular gratings using ebeam lithography, which is also tested using a bare Si wafer. The grating groove regions are defined in the positive ebeam resist ZEP using the JEOL JBX-9300FS EBL System. Some VP-SEM images of The resist patterns, taken by the Hitachi S-3700N VP-SEM, are shown in Fig. 4.7. It is observed that defects persist in all the circular grating patterns, resulting in rough outlines (Fig. 4.7(a)(b)). Some of the rectangular grating lines are straight and smooth (Fig. 4.7(c)), while others are displaced. This is because that the beam deflection amplifier of the current JEOL JBX-9300FS EBL System fails to accurately control the beam position. Since the circular grating lines are approximated using series of rectangular shapes, the amplifier failure increases the chance for the beam to miss the target positions. The stitching error of the current EBL system limits the GARC coupler fabrication. The process will be resumed once the new EBL system, Elionix ELS-G100, is ready for use. In the meanwhile, the feasibility of Nanoscribe laser lithography on grating patterning is tested. Figure 4.8 shows the VP-SEM image of the circular grating patterned in the negative Nanoscribe IP-Dip resist. It is observed that the

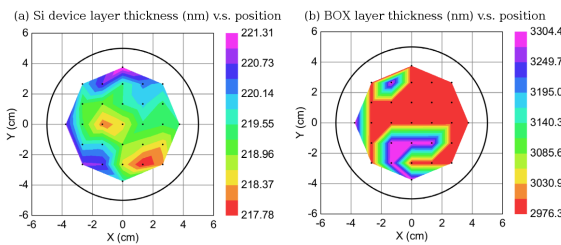


Figure 4.5: SOI film thicknesses characterized by Woollam M2000 Elipsometer.

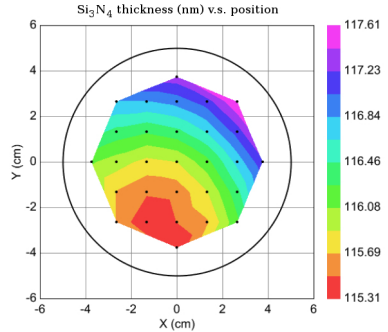


Figure 4.6: Si_3N_4 film thickness characterized by Woollam M2000 Elipsometer.

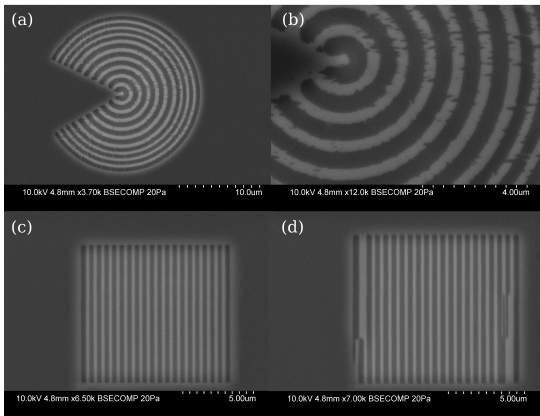


Figure 4.7: VP-SEM images of gratings defined in the positive ZEP resist by ebeam lithography.

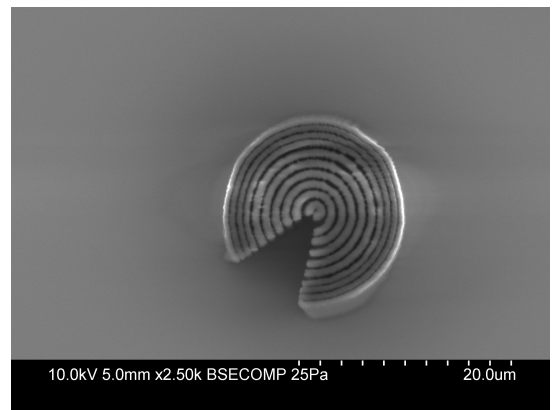


Figure 4.8: VP-SEM images of gratings defined in the negative IP-Dip resist by laser lithography.

circular grating ridges are not smooth, which is due to the fact that the laser beam moves in a straight line and circles are approximated in a staircase fashion. Nevertheless, the ridges can be made smoother by reducing the line spacing of the laser writing. The resist height can be adjusted so that the side wall of the circular grating is vertical. The circular gratings can be fabricated using the laser lithography because their grating periods are relatively large. However, it is preferred that the rectangular gratings can be simultaneously defined with the circular gratings in a single lithography step to simplify fabrication process, and thus EBL is the tool to use for grating patterning.

CHAPTER 5

PROPOSED WORK

The GARC couplers are a type of new interlayer coupling structure which have never been exploited before. The benefits of the GARC couplers, including but not limited to wide spectral bandwidth and high coupling efficiency, are only demonstrated by simulation, and thus the structure requires experimental validation and performance evaluation. Efficient fiber coupling is also important in order to introduce enough optical power into the GARC couplers and increase the signal-to-noise ratio in the coupling measurements. Rectangular diffraction gratings serve as the fiber couplers because the Floquet condition, which rectangular gratings follow, enables the fiber signal to diffract into the guided wave propagation direction. However, alignment of fiber to rectangular grating couplers has been a major bottleneck that limits the fiber coupling efficiency. As a result, a novel fiber alignment method need to be established. At a later stage, heterogeneous integration of 3D optical interconnects with electric interconnects is a promising platform to demonstrate.

5.1 Si/SiO₂ GARC Coupler Fabrication and Verification

The Si/SiO₂ GARC coupler will be fabricated following the process shown in Fig. 5.1. A SOI wafer with a 220 nm Si device layer and a 3 μm SiO₂ buried oxide layer is used as the substrate. The first step is to etch alignment marks into the SOI wafer. The alignment marks are patterned using Heidelberg Maskless aligner MLA150. The etch mask can be either a lifted-off chromium layer (step (a.1) to (a.4)) or a positive photoresist layer (e.g. SC1827). The exposed regions in the mask are etched sequentially using Cl₂ (Si etch) and using CF₄, O₂, and H₂ (SiO₂ etch) in Plasma Therm ICP, resulting in 2 μm deep trenches. After the etch mask is removed and substrate is cleaned, a 120 nm Si₃N₄ layer is deposited onto the substrate using LPCVD process in Tystar nitride furnace. Subsequent step involves

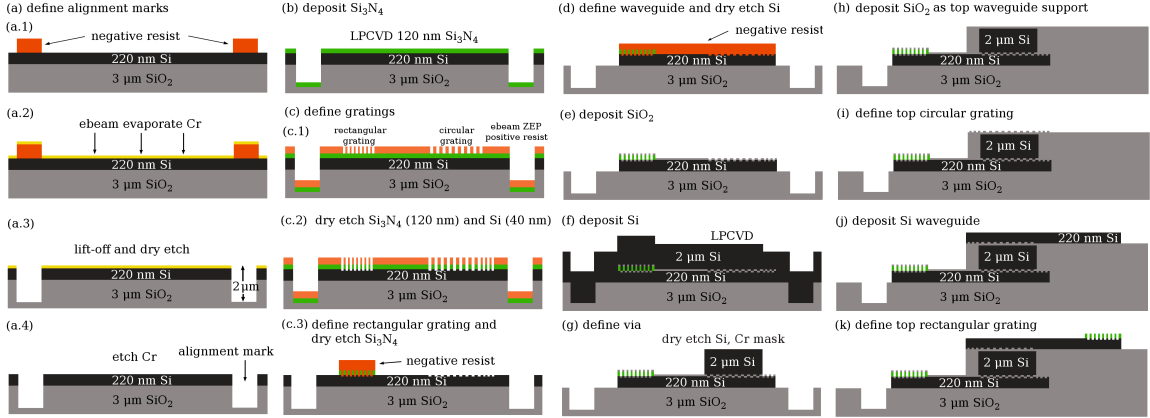


Figure 5.1: Fabrication steps for the Si/SiO₂ GARC coupler.

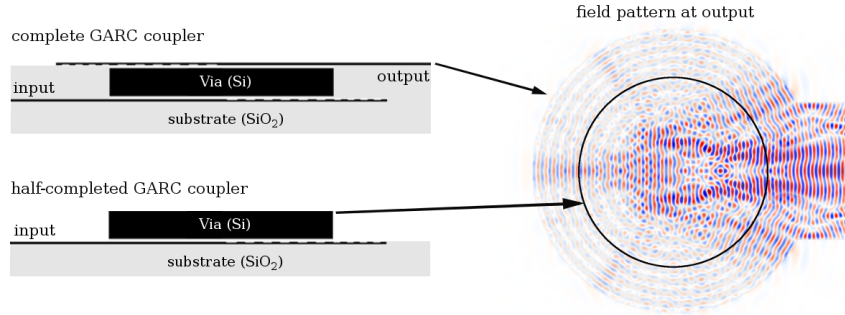


Figure 5.2: H_z field pattern at top of the via, assuming optical signal is launched from the bottom left waveguide. The field patterns at the top of the via are similar for the complete and half-completed structures.

circular and rectangular grating patterning using Elionix ELS-G100 EBL system. Then the Si₃N₄ layer is fully etched (same etching gas as for SiO₂) followed by 40 nm etch into the Si device layer to create the grating ridges, which is also carried out in Plasma Therm ICP. Then the rectangular grating regions are patterned and covered by negative photoresist (e.g. NR9-1500y) and the uncovered Si₃N₄ regions are etched. A similar process is used to isolate the whole waveguide structures by fully etching the Si device layer. Then the SiO₂ thin layer can be CVD-deposited or sputtered, depending on further investigations of the film quality. Subsequently, a 2 μ m Si layer is LPCVD-deposited using Tystar poly furnace, followed by ICP etching to define the Si via.

A preliminary verification can be carried out in the half way of the process after the Si

via is defined. Since the via functions as a resonant cavity and only a portion of its power leaks out through the SiO_2 thin layer, the field pattern at the top of the via should be similar to the simulated field pattern as shown in Fig. 5.2. After introducing optical signal into the bottom input waveguide, the field pattern on the top of the via can be imaged by an IR camera or a visible light camera by the assistant of upconversion nanoparticles, e.g. Er doped NaYF_4 , which convert IR light into visible spectrum. The image can be compared with the simulated field pattern to approximate the resonance behavior of the via. Complete coupling efficiency and spectral response measurements can be conducted using a tunable laser and a power meter after the entire GARC coupler is fabricated. Finally, the GARC coupler will be integrated into the electrical HIST platform [44].

5.2 Innovative Fiber Alignment Fixture Design and Fabrication

The fiber-optic alignment involves six degrees of freedom, namely translational (x, y, z) and rotational (pitch, yaw, roll). Efficient fiber-to-grating coupling requires $\pm 200 \text{ nm}$ accuracy in translational directions and a few degrees accuracy (e.g. 3°) in the rotation angles to ensure less than 1 dB loss [45]. There exist two types of fiber alignment techniques, namely active alignment (using a laser input and measuring the output intensity) and passive alignment (using a flip-chip bonder or a microscope). No matter which technique is used, fiber has to be aligned one at a time, making the whole process tedious. Epoxy glue is commonly used to mount the fiber after the alignment, which bounds the fiber and the chip and requires extra effort to remove it. To solve these problems, a multi-use fiber alignment fixture will be designed based on the positive self-alignment structures (PSAS) concept. The PSAS allows sub-micron alignment accuracy and it can be used as a scaffold for the fiber alignment fixture. Finer adjustments in translational and rotational directions can be further investigated. By properly design the fixture, fiber arrays can be aligned simultaneously. The fixture can be easily removed from the chip and allows for multi-chip testing.

REFERENCES

- [1] M. Glick, L. C. Kimmerling, and R. C. Pfahl, “A roadmap for integrated photonics,” *Opt. Photon. News*, vol. 29, no. 3, pp. 36–41, 2018.
- [2] R. Halir, A. Ortega-Monux, J. H. Schmid, C. Alonso-Ramos, J. Lapointe, D. X. Xu, J. G. Wanguemert-Perez, I. Molina-Fernandez, and S. Janz, “Recent advances in silicon waveguide devices using sub-wavelength gratings,” *IEEE J. Sel. Top. Quantum Electron.*, vol. 20, no. 4, pp. 279–291, 2014.
- [3] J. Kang, Y. Atsumi, M. Oda, T. Amemiya, N. Nishiyama, and S. Arai, “Layer-to-layer grating coupler based on hydrogenated amorphous silicon for three-dimensional optical circuits,” *Jpn. J. Appl. Phys.*, vol. 51, no. 12R, p. 120203, 2012.
- [4] Y. Tang, D. Dai, and S. He, “Proposal for a grating waveguide serving as both a polarization splitter and an efficient coupler for silicon-on-insulator nanophotonic circuits,” *IEEE Photon. Technol. Lett.*, vol. 21, no. 4, pp. 242–244, 2009.
- [5] O. Solgaard, F. S. A. Sandejas, and D. M. Bloom, “Deformable grating optical modulator,” *Opt. Lett.*, vol. 17, no. 9, pp. 688–690, 1992.
- [6] Y. Shibata, S. Oku, Y. Kondo, T. Tamamura, and M. Naganuma, “Semiconductor monolithic wavelength selective router using a grating switch integrated with a directional coupler,” *J. Lightwave Technol.*, vol. 14, no. 6, pp. 1027–1032, 1996.
- [7] G. Li, Y. Hashimoto, T. Maruyama, and K. Iiyama, “High-efficiency optical coupling to planar photodiode using metal reflector loaded waveguide grating coupler,” *Opt. Quant. Electron.*, vol. 45, no. 7, pp. 657–663, 2013.
- [8] S. R. Park, O. J. Kwon, D. Shin, S.-H. Song, H.-S. Lee, and H. Y. Choi, “Grating micro-dot patterned light guide plates for LED backlights,” *Opt. Express*, vol. 15, no. 6, pp. 2888–2899, 2007.
- [9] K. M. Byun, S. J. Kim, and D. Kim, “Grating-coupled transmission-type surface plasmon resonance sensors based on dielectric and metallic gratings,” *Appl. Opt.*, vol. 46, no. 23, pp. 5703–5708, 2007.
- [10] M.-S. Kwon, “Disposable and compact integrated plasmonic sensor using a long-period grating,” *Opt. Lett.*, vol. 35, no. 22, pp. 3835–3837, 2010.

- [11] N. Eriksson, M. Hagberg, and A. Larsson, “Highly directional grating outcouplers with tailorable radiation characteristics,” *IEEE J. Quantum Electron.*, vol. 32, no. 6, pp. 1038–1047, 1996.
- [12] S. H. Lin, K. Y. Hsu, W.-Z. Chen, and W. T. Whang, “Phenanthrenequinone-doped poly (methyl methacrylate) photopolymer bulk for volume holographic data storage,” *Opt. Lett.*, vol. 25, no. 7, pp. 451–453, 2000.
- [13] C. Gu, H. Fu, and J. R. Lien, “Correlation patterns and cross-talk noise in volume holographic optical correlators,” *J. Opt. Soc. Am. A*, vol. 12, no. 5, pp. 861–868, 1995.
- [14] C. C. Sun and W. C. Su, “Three-dimensional shifting selectivity of random phase encoding in volume holograms,” *Appl. Opt.*, vol. 40, no. 8, pp. 1253–1260, 2001.
- [15] K. O. Hill and G. Meltz, “Fiber Bragg grating technology fundamentals and overview,” *J. Lightwave Technol.*, vol. 15, no. 8, pp. 1263–1276, 1997.
- [16] J. M. Tedesco, H. Owen, D. M. Pallister, and M. D. Morris, “Principles and spectroscopic applications of volume holographic optics,” *Anal. Chem.*, vol. 65, no. 9, 441A–449A, 1993.
- [17] R Petit, *Electromagnetics Theory of Gratings*. Springer-Verlag, 1980.
- [18] R.-S. Chu and J. A. Kong, “Modal theory of spatially periodic media,” *IEEE Trans. Microwave Theory Tech.*, vol. 25, no. 1, pp. 18–24, 1977.
- [19] T. K. Gaylord and M. G. Moharam, “Analysis and applications of optical diffraction by gratings,” *Proc. IEEE*, vol. 73, no. 5, pp. 894–937, 1985.
- [20] S. T. Peng, T. Tamir, and H. L. Bertoni, “Theory of periodic dielect waveguides,” *IEEE Trans. Microwave Theory Tech.*, vol. 23, no. 1, pp. 123–133, 1975.
- [21] H. Kogelnik, “Coupled wave theory for thick hologram gratings,” *Bell Syst. Tech. J.*, vol. 48, no. 9, pp. 2909–2947, 1969.
- [22] W. Streifer, D. Scifres, and R. Burnham, “Analysis of grating-coupled radiation in GaAs: GaAlAs lasers and waveguides-I,” *IEEE J. Quantum Electron.*, vol. 12, no. 7, pp. 422–428, 1976.
- [23] A. Yariv, “Coupled-mode theory for guided-wave optics,” *IEEE J. Quantum Electron.*, vol. 9, no. 9, pp. 919–933, 1973.

- [24] C. Wan, T. K. Gaylord, and M. S. Bakir, “Grating design for interlayer optical interconnection of in-plane waveguides,” *Appl. Opt.*, vol. 55, no. 10, pp. 2601–2610, 2016.
- [25] G. Roelkens, D. Vermeulen, D. Van Thourhout, R. Baets, S. Brision, P. Lyan, P. Gautier, and J.-M. Fedeli, “High efficiency diffractive grating couplers for interfacing a single mode optical fiber with a nanophotonic silicon-on-insulator waveguide circuit,” *Appl. Phys. Lett.*, vol. 92, no. 13, p. 131 101, 2008.
- [26] C. Wan, T. K. Gaylord, and M. S. Bakir, “RCWA-EIS method for interlayer grating coupling,” *Appl. Opt.*, vol. 55, no. 22, pp. 5900–5908, 2016.
- [27] G. Roelkens, D. Vermeulen, S. Selvaraja, R. Halir, W. Bogaerts, and D. Van Thourhout, “Grating-based optical fiber interfaces for silicon-on-insulator photonic integrated circuits,” *IEEE J. Sel. Top. Quantum Electron.*, vol. 17, no. 3, pp. 571–580, 2011.
- [28] X. Chen, C. Li, C. K. Fung, S. M. Lo, and H. K. Tsang, “Apodized waveguide grating couplers for efficient coupling to optical fibers,” *IEEE Photon. Technol. Lett.*, vol. 22, no. 15, pp. 1156–1158, 2010.
- [29] D. Taillaert, W. Bogaerts, P. Bienstman, T. F. Krauss, P. V. Daele, I. Moerman, S. Verstuyft, K. D. Mesel, and R. Baets, “An out-of-plane grating coupler for efficient butt-coupling between compact planar waveguides and single-mode fibers,” *IEEE J. Quantum Electron.*, vol. 38, no. 7, pp. 949–955, 2002.
- [30] M. Dai, L. Ma, Y. Xu, M. Lu, X. Liu, and Y. Chen, “Highly efficient and perfectly vertical chip-to-fiber dual-layer grating coupler,” *Opt. Express*, vol. 23, no. 2, pp. 1691–1698, 2015.
- [31] D. Benedikovic, C. Alonso-Ramos, P. Cheben, J. H. Schmid, S. Wang, D.-X. Xu, J. Lapointe, S. Janz, R. Halir, A. Ortega-Moñux, J. Fedeli, S. Janz, I. Molina-Fernandez, and M. Dado, “High-directionality fiber-chip grating coupler with interleaved trenches and subwavelength index-matching structure,” *Opt. Lett.*, vol. 40, no. 18, pp. 4190–4193, 2015.
- [32] T. Watanabe, M. Ayata, U. Koch, Y. Fedoryshyn, and J. Leuthold, “Perpendicular grating coupler based on a blazed antiback-reflection structure,” *IEEE J. Lightwave Technol.*, vol. 35, no. 21, pp. 4663–4669, 2017.
- [33] F. Van Laere, T. Claes, J. Schrauwen, S. Scheerlinck, W. Bogaerts, D. Taillaert, L. O’Faolain, D. Van Thourhout, and R. Baets, “Compact focusing grating couplers for silicon-on-insulator integrated circuits,” *IEEE Photon. Technol. Lett.*, vol. 19, no. 23, pp. 1919–1921, 2007.

- [34] S. M. Schultz, E. N. Glytsis, and T. K. Gaylord, “Design of a high-efficiency volume grating coupler for line focusing,” *Appl. Opt.*, vol. 37, no. 12, pp. 2278–2287, 1998.
- [35] M. G. Moharam, E. B. Grann, D. A. Pommet, and T. K. Gaylord, “Formulation for stable and efficient implementation of the rigorous coupled-wave analysis of binary gratings,” *J. Opt. Soc. Am. A*, vol. 12, pp. 1068–1076, 1995.
- [36] E. Anemogiannis and E. N. Glytsis, “Multilayer waveguides: efficient numerical analysis of general structures,” *J. Lightwave Technol.*, vol. 10, pp. 1344–1351, 1992.
- [37] M. Cabezón, I. Garcés, A. Villafranca, J. Pozo, P. Kumar, and A. Kaźmierczak, “Silicon-on-insulator chip-to-chip coupling via out-of-plane or vertical grating couplers,” *Appl. Opt.*, vol. 51, pp. 8090–8094, 2012.
- [38] S. Bernabé, C. Kopp, M. Volpert, J. Harduin, J. M. Fédéli, and H. Ribot, “Chip-to-chip optical interconnections between stacked self-aligned soi photonic chips,” *Opt. Express*, vol. 20, pp. 7886–7894, 2012.
- [39] A. V. Mulé, R. Villalaz, T. K. Gaylord, and J. D. Meindl, “Quasi-free-space optical coupling between diffraction grating couplers fabricated on independent substrates,” *Appl. Opt.*, vol. 43, pp. 5468–5475, 2004.
- [40] C. Wan, T. K. Gaylord, and M. S. Bakir, “Rigorous coupled-wave analysis equivalent-index-slab method for analyzing 3d angular misalignment in interlayer grating couplers,” *Appl. Opt.*, vol. 55, no. 35, pp. 10 006–10 015, 2016.
- [41] ——, “Circular waveguide grating-via-grating for interlayer coupling,” *IEEE Photon. Technol. Lett.*, vol. 29, no. 21, pp. 1776–1779, 2017.
- [42] F. Van Laere, G. Roelkens, M. Ayre, J. Schrauwen, D. Taillaert, D. Van Thourhout, T. F. Krauss, and R Baets, “Compact and highly efficient grating couplers between optical fiber and nanophotonic waveguides,” *IEEE J. Lightwave Technol.*, vol. 25, no. 1, pp. 151–156, 2007.
- [43] D. M. Pozar, “Circular waveguide cavity resonators,” in *Microwave Engineering*, Wiley, 2011, ch. 6.4, pp. 288–292.
- [44] X. Zhang, P. K. Jo, M. Zia, G. S. May, and M. S. Bakir, “Heterogeneous interconnect stitching technology with compressible microinterconnects for dense multi-die integration,” *IEEE Electron Device Lett.*, vol. 38, no. 2, pp. 255–257, 2017.
- [45] Z Tang, R Zhang, S. Mondal, and F. Shi, “Optimization of fiber-optic coupling and alignment tolerance for coupling between a laser diode and a wedged single-mode fiber,” *Opt. Commun.*, vol. 199, no. 1-4, pp. 95–101, 2001.